Space Science Review manuscript No.
(DOI 10.1007/s11214-017-0330-3)

Thermosphere-Ionosphere-Electrodynamics General Circulation Model for the Ionospheric Connection Explorer: TIEGCM-ICON

Astrid Maute

Received: 3 October 2016 / Accepted: 4 January 2017

Abstract **Keywords** numerical modeling · ICON explorer · atmospheric tides

The NASA Ionospheric Connection explorer (ICON) will study the coupling between the thermosphere and ionosphere at low- and mid-latitudes by measuring the key parameters. The ICON mission will also employ numerical modeling to support the interpretation of the observations, and examine the importance of different vertical coupling mechanisms by conducting numerical experiments. One of these models is the Thermosphere-Ionosphere-Electrodynamics General Circulation Model-ICON (TIEGCM-ICON) which will be driven by tidal perturbations derived from ICON observations using the Hough Mode Extension method (HME) and at high latitude by ion convection and auroral particle precipitation patterns from the Assimilative Mapping of Ionospheric Electrodynamics (AMIE). The TIEGCM-ICON will simulate the thermosphere-ionosphere (TI) system during the period of the ICON mission. In this report the TIEGCM-ICON is introduced, and the focus is on examining the effect of the lower boundary on the TI-system to provide some guidance for interpreting future ICON model results.

1 Introduction

The Ionospheric Connection explorer (ICON) will study the coupling between the thermosphere and ionosphere at low- and mid-latitudes. The science questions (SQ) which ICON will address are (1) What causes changes in the ionosphere, other than geomagnetic effects?, (2) How do large-scale atmospheric waves control the ionosphere at low latitudes?, and (3) How do ion-neutral coupling processes respond to increases in solar forcing and geomagnetic activity? The ICON mission will measure key coupling quantities such as the neutral wind, temperature and composition, the electric field/ion drift and plasma density, and will employ numerical modeling informed by the measurements to investigate the SQs. Although modeling will be used in all SQs we focus on SQ (2) since this motivated the TIEGCM-ICON model development described in the following.

A. Maute
P.O. Box 3000, Boulder CO 80307
Tel.: +1303-497-1539
Fax: +1303-497-1589
E-mail: maute@ucar.edu

In the last two decades, progress in understanding the coupling of the lower atmosphere to the TI system could be made due to the increase in observations and improved modeling capabilities. The influence of lower atmospheric waves which can propagate up into the lower thermosphere and imprint their longitudinal variations on the plasma distribution was demonstrated. Wave type features were observed in the ionosphere (e.g., *Immel et al.*, 2006; *Lin et al.*, 2007; *Liu and Watanabe*, 2008; *Liu et al.*, 2011; *Burns et al.*, 2012), in the electric field and ion drifts (e.g., *Kil et al.*, 2007; *Fejer et al.*, 2008), the equatorial electrojet (e.g., *Lühr et al.*, 2004; *Le Mouël et al.*, 2006; *Alken et al.*, 2013), the thermospheric wind (e.g., *Oberheide et al.*, 2011a; *Häusler et al.*, 2010, 2015), neutral mass density (e.g., *Liu et al.*, 2009) and neutral composition (e.g., *Zhang et al.*, 2010; *Kil and Paxton*, 2011). With the help of numerical modeling possible mechanisms for the vertical coupling were examined (e.g., *England et al.*, 2010; *Jin et al.*, 2011; *Liu et al.*, 2013; *Jones et al.*, 2014; *Pedatella et al.*, 2016). The importance of the electrodynamic coupling caused by waves propagating into the E-region and modifying the electric field and ion drift was examined by e.g., *England et al.* (2010); *Kil et al.* (2007). It was also shown that some waves are able to propagate into the F-region (e.g., *Häusler and Lühr*, 2009; *Oberheide et al.*, 2011b) and may directly influence the plasma distribution. The tidal effect on the mean circulation and on modifying the neutral composition were investigated by e.g., *Yamazaki and Richmond* (2013); *Jones et al.* (2014); *Pedatella and Maute* (2015). The comparative importance of these different mechanisms is still not fully understood, and a comprehensive set of measurements to verify the mechanisms is still missing.

To provide some context a brief overview of the ICON modeling effort pertaining to the thermosphere-ionosphere-electrodynamic general circulation model (TIEGCM) is given. An ICON adapted version of the TIEGCM will be employed during the ICON mission to simulate the TI-system. Crucial in examining the vertical coupling are realistic tidal specifications at the lower boundary (LB) of the TIEGCM. The LB specifications will be derived from the ICON wind and temperature measurements using the Hough Mode Extension (HME) method (e.g., *Forbes and Hagan*, 1982; *Oberheide et al.*, 2011b). Due to the precession of the ICON satellite 27 days of measurements are needed to capture all longitudes and local times and determine the zonal wave number and period of waves. Therefore the HME tidal perturbations represent a 27 day “average” which is updated every day. The effects of the satellite flight orbit on the HME tidal specifications are not discussed herein. Realistic magnetosphere-ionosphere coupling at TIEGCM high latitude will be provided by the Assimilative Mapping of Ionospheric Electrodynamics (AMIE) with particle precipitation and ion convection patterns. The AMIE-ICON is not the focus of the current study.

In the following we will focus on the TIEGCM modeling component and examine the influence of the lower boundary specifications on the TI-system. In section 2 the TIEGCM-ICON is described, which is based on the TIEGCM V2.0 released in March 2016 and described in section 2.1. The TIEGCM modifications for the ICON project are specified in section 2.2. The TIEGCM-ICON simulations are introduced in section 3, and the TI-effects due to the changes in the lower boundary forcing are presented in section 4 and discussed in section 5. The paper concludes with a summary in section 6.

2 TIEGCM

The TIEGCM is a self consistent numerical model of the thermosphere which includes the dynamics, energetics and chemistry with a steady-state ionospheric electrodynamo in a realistic geomagnetic main field defined by the International Geomagnetic Reference Field

(IGRF-12) (*Thébault et al.*, 2015). The original development was done by *Dickinson et al.* (1984); *Roble et al.* (1988); *Richmond et al.* (1992) and the interested reader can get more information about the more recent TIEGCM model in e.g., *Qian et al.* (2014); *Richmond and Maute* (2013) and references therein.

The model spans from approximately 97 km to 450 to 600 km depending on the solar cycle. The TIEGCM uses log pressure $Z = ln(p_0/p)$ as the vertical coordinate with the reference pressure p_0 set to $p_0 = 5 \times 10^7 hPa$. For the ICON mission the model resolution will be set to 2.5^o by 2.5^o in geographic longitude and latitude and four grid points per scale height in the vertical. The ionospheric electrodynamics are calculated in a modified aagnetic Apex coordinate system (*Richmond*, 1995). Magnetic longitude and latitude are constant along geomagnetic-field lines and at the 90 km reference height, the magnetic grid spacing is 4.5^o in magnetic longitude and between 0.34^o to 3.07^o in magnetic latitude from the equator to the poles.

In the TIEGCM the solar XUV, EUV, and FUV spectral fluxes are defined by the EUVAC model (*Richards et al.*, 1994) using the observed F10.7 index. The high latitude energy input associated with auroral particle precipitation is either calculated by an analytical auroral model (*Roble and Ridley*, 1987; *Emery et al.*, 2012) or defined by the AMIE procedure.

The TIEGCM ionospheric electrodynamo solves for the global electric potential due to the wind dynamo at middle and low latitude. At high latitudes the electric potential is prescribed by e.g., *Weimer* (2005); *Heelis et al.* (1982) or AMIE patterns. To merge the region of the wind dynamo with the high latitude region a cross-over boundary is introduced which varies dynamically with the strength of the magnetospheric forcing. In the TIEGCM the merging region extends over a 15^o magnetic latitude range and starts 5^o equatorward of the ion convection reversal boundary (*Solomon et al.*, 2012).

2.1 TIEGCM V2.0

The TIEGCM-ICON is based on the TIEGCM V2.0 which was released in March 2016. In the following we will briefly describe ICON relevant new features. For more details about TIEGCM V2.0 we refer the reader to the website at http://www.hao.ucar.edu/modeling/tgcm/tiegcm2.0.

In TIEGCM V2.0 Helium is treated as a major species as the default, and will be used in the TIEGCM-ICON. The changes to the continuity equation, the molecular, thermal and eddy diffusion and the compositional equation are described by *Sutton et al.* (2015). The helium mass mixing ratio ψ_{he} has to be considered when calculating the mean mass and scale height. At the lower boundary ($Z = -7$; approximately at 97 km) ψ_{he} is set to 1.154×10^{-6}. At the TIEGCM upper boundary (Z=7) the diffusive flux of O and He is balanced globally. Helium can become a dominant species close to the TIEGCM upper boundary especially in the solstice winter hemisphere (*Sutton et al.*, 2015).

The ionospheric electrodynamo was parallized in longitude and latitude using the Message Passing Interface (MPI) and the Earth System Modeling Framework (ESMF) for the mapping between the geographic and the geomagnetic coordinate systems. The speed up is around 50% for the 2.5^o resolution on the 64 processors NSF/NCAR yellowstone system.

In the TIEGCM gravity g is constant with $g = 8.7 m/s^2$ and is used to determine the geopotential height at a pressure level. For the comparison with the ICON observations the geometric height will be used. The geometric height is calculated by assuming that gravity decreases from the constant reference value at the lower boundary.

In the TIEGCM V2.0 the filters have been adjusted. Details about the different filters can be found on the TIEGCM V2.0 website. Spatial filters were modified for the 2.5^o grid resolution. A filter applied in time (called ”Shapiro filter”) was adjusted to the default 30 sec time step size for the 2.5^o grid resolution and adapts to time step size changes by varying a filter factor. For the TIEGCM-ICON a constant time step size of 10 secs will be used. This will allow the model to simulate geomagnetic disturbed periods and avoid stability problems.

2.2 TIEGCM-ICON

The modifications of the TIEGCM V2.0 leading to the TIEGCM-ICON are described in the following. The TIEGCM-ICON will simulate the TI system for the mission period with a few weeks' time lag. Therefore, some advanced features available in the TIEGCM V2.0 will not be used in the baseline simulation e.g., solar irradiance based on TIMED/SEE data. *Fang et al.* (2008) compared daytime TIEGCM electron density in the E-region with the International Reference Ionosphere (IRI) finding 30-40% smaller E-region densities. They increased the soft X-ray fluxes in the 8-40 Å wavelength range by a factor of 4.4 to better match the IRI E-region plasma densities. When addressing the ICON SQs it is important to get realistic E-region plasma density magnitudes since these will influence the conductivities in the wind dynamo region and in general lead to an increase of the E-region dynamo contributions. The TIEGCM-ICON adapted the modifications suggested by *Fang et al.* (2008), which were already applied in several studies (e.g., *Maute et al.*, 2012; *Yamazaki et al.*, 2014; *Jones et al.*, 2014, 2016).

The TIEGCM includes the effect of upward propagating tides by specifying the tidal perturbations at the TIEGCM lower boundary. The perturbations are defined in the geopotential height, neutral temperature and horizontal winds and added to the zonally and diurnally averaged corresponding quantities. In the following we will refer to the zonally and diurnally averaged values as the “background”.

The default TIEGCM lower boundary (LB) background is assumed to be constant with a neutral temperature $T_{zm} = 181K$, geopotential height $z_{zm} = 96.37$ km, and zero horizontal winds. *Jones et al.* (2014) compared these background conditions to the climatology from Mass Spectrometer Incoherent Scatter Radar Extended (MSISE00) (*Picone et al.*, 2002) and the horizontal wind model (HWM07) (*Drob et al.*, 2008) and found significant latitudinal and seasonal variations not captured by the default TIEGCM LB background. Tidal propagation is influenced by the atmospheric background conditions and therefore a realistic background is desirable.

We follow the approach of *Jones et al.* (2014) and employ their monthly climatology at the TIEGCM lower boundary. The monthly climatology is assumed to be at the middle of each month and is illustrated in Figure 1. Values are linearly interpolated in time. These TIEGCM-ICON modifications are available in TIEGCM V2.0. Dr. Jones Jr. produced updated climatological lower boundary conditions by replacing HWM07 with HWM14 (*Drob et al.*, 2015) which were tested in TIEGCM-ICON. It was found that the influence of horizontal wind climatology at the lower boundary based on HWM07 versus HWM14 on the TI state is not significant, and therefore the published lower boundary climatology with HWM07 was employed (*Jones et al.*, 2014).

Important for the ICON modeling effort is *Jones et al.* (2014)'s conclusion that the TIEGCM with the modified lower boundary background can reproduce the tidal propagation reasonably well in the dynamo E-region when compared to thermosphere-ionosphere-mesosphere-electrodynamics general circulation model (TIMEGCM) results (lower boundary at approximately 30 km).

The tidal perturbations at the TIEGCM-ICON lower boundary will be derived from ICON observations using the Hough Mode Extension (HME) technique. The TIEGCM-ICON was modified to be able to read in daily HME files with hourly (from 0 to 23 UT) global perturbations in geopotential height, temperature and horizontal winds. The values are linearly interpolated in time.

The TIEGCM-ICON includes the option to specify hourly perturbations at the lower boundary from any source via files. Although this will not be used during the ICON mission it is helpful for testing the influence of the lower boundary perturbations on the TI-system. In the following we will employ this lower boundary option as a substitute for the HME LB conditions to study the TIEGCM-ICON.

3 TIEGCM-ICON simulations

The 2009 TIMEGCM simulation described by *Häusler et al.* (2015) is used to define the TIEGCM lower boundary. We will conduct numerical experiments by performing three simulations with varying lower boundary conditions: (1) daily varying background and perturbations based on TIMEGCM (for short: DPDB), (2) daily varying perturbations based on TIMEGCM and climatological background (for short: DPCB), and (3) 27 day averaged diurnal perturbations based on TIMEGCM and climatological background (for short: 27PCB). The difference between simulation (1) and (2) quantifies the effect of using a background climatology while the comparison of simulations (2) and (3) illustrates the effect of a 27 day averaged diurnal LB perturbation on the TI-system. The simulation are for the solar minimum year 2009. The 3-hourly Kp index and daily solar flux is presented in Figure 2. The magnetosphere-ionosphere coupling is simulated by employing the empirical *Heelis et al.* (1982) ion convection pattern and the default auroral particle precipitation both parametrized by the 3-hourly K_p index (*Emery et al.*, 2012).

The background based on the TIMEGCM simulation at pressure level Z=-7 are depicted in Figure 3. Note that the color scale in Figure 1 and Figure 3 differ, and that the former represents a climatology while the latter represents the 2009 conditions. The seasonal variation in the temperature and geopotential height is similar in the climatology and 2009 background although the magnitude differs.

The TIEGCM-ICON lower boundary perturbations are based on the 2009 TIMEGCM simulation. The perturbations are determined by removing the zonal and diurnal mean from the TIMEGCM geopotential height, temperature and horizontal wind at pressure level Z=-7. Due to the processing method the perturbations are not limited to solar atmospheric tides and can include other waves e.g., planetary waves. The main solar atmospheric tidal components at the lower boundary based on hourly values of the daily diurnal variation and of the 27-day averaged diurnal variation are depicted in Figure 4 on the right and left side, respectively.

The solar tidal nomenclature we will be using from hereafter is D for diurnal (period of 24 hrs; p=24), S for semidiurnal (p=12 hrs), and T for terdiurnal (p=8 hrs), and W for westward propagating tides (zonal wave number $s < 0$), and E for eastward propagating tides ($s > 0$). The main solar tides presented from the top downward are DW1, SW2, TW3, DE3, and DE2. The neutral temperature amplitude of the 27 day diurnal average captures all the main variations in the illustrated components. As expected the peak amplitudes are in general lower for the 27 day averaged diurnal LB perturbation (left side) than for the daily variations (right side).

4 Effects on the thermosphere-ionosphere system

4.1 Solar atmospheric tides

We compare the solar tidal amplitude and phase of different components in the E-region at approximately 120 km (Z=-4.125) in Figure 5 and Figure 6, respectively. The tidal amplitude and phase were determined by least square fitting using the diurnal variation with hourly values.

The tidal amplitude variations (Figure 5) from the 3 simulations all capture similar seasonal and latitudinal variations. As expected the day-to-day variability is increased when daily varying LB perturbations are applied (case DPCB and DPDB). However the daily varying LB background (DPDB) does not seem to enhance the tidal amplitude variability. The maximum amplitudes for the different tidal components are similar in the three simulation indicating that the 27PCB can represent the variations on time scales longer than 8-10 days.

In Figure 6 the associated phase variations of the tidal components are illustrated. The tidal phase variations for the 3 simulations agree well.

The tidal amplitudes around 300 km are illustrated in Figure 7. At this altitude the migrating diurnal component DW1 dominates due to the in-situ solar forcing. Most temporal and latitudinal amplitude variations agree reasonably well between the different simulations. A difference can be recognized during the northern summer when DW1 amplitude in the DPDB simulation is smaller than in the other two simulations while SW2 tends to be larger during the same period. The in-situ forcing due to solar radiation is the same in the 3 simulations suggesting that the upward propagating tidal components differ in each case. However no consistent differences in the tidal amplitudes between the 27PCB case and the other two cases can be noted indicating that the tidal propagation agrees reasonably well between the simulations.

Examining the zonal wind tidal variations (not shown) leads to similar conclusions as for the neutral temperature. In the E-region the zonal wind amplitudes of the three simulations exhibit similar seasonal and latitudinal variations with no systematic difference in the magnitude of the amplitude. In the F-region during northern hemisphere summer zonal wind DW1 amplitude of the DPDB case is slightly reduced compared to the DPCB and 27PCB cases while the SW2 amplitude is somewhat stronger. This behavior is also observed in the neutral temperature amplitudes although it is less pronounced in the zonal wind.

The temperature amplitude variations at 300 km can be compared with the GOCE/CHAMP observations as well as TIMEGCM results at 340 km published by *Häusler et al.* (2015). The TIEGCM-ICON neutral temperature amplitudes compare favorably with the TIMEGCM simulation (*Häusler et al.*, 2015). TIMEGCM exhibits the same low DW1 amplitudes during northern summer as the DPDB simulation. Also the temporal variation and latitudinal structure of SW2 and TW3 are similar in TIEGCM-ICON and TIMEGCM. Since the TIMEGCM and TIEGCM-ICON behaves similarly we refer to *Häusler et al.* (2015) for a discussion about the comparison of TIMEGCM results to the CHAMP/GRACE derived temperature amplitudes.

4.2 Equatorial vertical ExB drift

The daytime low latitude ionospheric plasma distribution is influenced by the equatorial vertical ExB drift. The local time variation of the vertical ExB drift over day of the year (doy) at the magnetic equator (geographic longitude $\phi = 15^o$ and geographic latitude $\lambda = 11^o$) is illustrated in Figure 8. The 27PCB simulation captures the main daytime variations over the year although the daytime drifts tend to be smaller than in the other two simulations. For an easier comparison the yearly mean diurnal vertical ExB drift variation is depicted in Figure 9. The darker colored lines represent the yearly mean while the corresponding lighter color shaded area presents the standard deviation.

Overall the diurnal variation of the upward vertical ExB drift is captured. The mean vertical drift of the three simulations is mostly within the standard deviations. The mean daytime vertical ExB drift for the simulations with daily varying LB perturbations (DPDB & DPCB) are slightly higher than for the 27 day averaged diurnal LB perturbations (27PCB), and the daytime peak of DPDB tend to occur at later local time (around 11 LT versus 9-10 LT) . As expected the 27PCB simulation has a smaller standard deviation especially during the daytime, indicating that part of the temporal variability is related to the lower boundary perturbation variations.

The average longitudinal variation of the vertical ExB drift for different local times at the geomagnetic equator is depicted in Figure 10 for four 15-day time periods in January, March, July and September. The daytime longitudinal variation at low latitude is mainly driven by atmospheric tides through the ionospheric wind dynamo. Overall the longitudinal variations of the 3 simulations is similar however the 27PCB case tends to have lower vertical drifts during doy 180-195 period in the sector around 0^o geographic longitude. A possible cause may be the slight modification in the tidal spectrum as indicated by the selected tidal amplitudes in Figures 5 and 7. The effect of the modified winds can be further modulated by the geomagnetic main field variations (e.g., *Maute et al.*, 2012). Detailed examination of the longitudinal variations is not within the purview of the present TIEGCM-ICON study.

To assess the simulations we compare briefly with published results. *Stoneback et al.* (2011) analyzed Coupled Ion Neutral Dynamics Investigation (CINDI) Ion Velocity Meter (IVM) data onboard the Communication/Navigation Outage Forecasting System (C/NOFS) satellite to derive vertical ion drifts from late 2008 to 2010 for different seasons and longitudinal sectors. The CINDI observations are from a 400-550 km altitude range while the simulations are at pressure level Z=2 (approximately 260 km). *Hui and Fejer* (2015) demonstrated that the vertical drift does not vary significantly with height which allows us to compare the observed vertical ion drifts with the simulated ExB drifts.

Overall the simulated yearly mean daytime vertical drift maximum is smaller than the mostly 30-40 m/s observed drift. The local time of the observed daytime peak varies from 9 local time (LT) in spring 2009, 10-11 LT in northern summer and winter 2009 and almost 12 LT in Fall 2009. In the simulations the mean daytime peak is not very distinct and between 10-11 LT.

Small or downward vertical drifts were observed in the late afternoon (16-18 LT) in most seasons in the $0^o - 60^o$ longitudinal sector. The simulations do not show negative mean drifts in the afternoon at 15^o longitude but rather around -60^o to 0^o and 60^o to 120^o longitude especially for the periods of doy 15-30 and doy 180-195 (see Figure 10).

During solar minimum conditions the prereversal enhancement (PRE) is very weak or not occurring. During the 2009 equinox conditions weak PRE based on C/NOFS observations were found in some longitudinal sector (-180^o to -120^o, and 120^o to 180^o) (*Stoneback et al.*, 2011) which the 27PCB model can partly reproduce. In the early morning (4-6LT) strong downward drift of roughly 20-40 m/s were sometimes observed by C/NOFS. The longitudinal variation of these early morning downward drift was captured by ROCSAT-1 (*Fejer et al.*, 2008) with strongest downward drift in the -75^o to 90^o longitudinal sector. The 27PCB simulation can reproduce the main longitudinal variation of the downward drift.

4.3 Ionospheric plasma distribution

The ionospheric plasma distribution can be characterized by NmF2 and hmF2, the F-region peak plasma density and associated height, respectively. In Figure 11 the variation of NmF2 (left) and hmF2 (right) at 13 LT (12 universal time (UT) and $\phi = 15^o$ geographic longitude) is depicted for the three simulations. All the simulations have similar seasonal variations at low- and mid-latitude with smaller NmF2 during June-August and higher NmF2 for the months of September to March. However the magnitude of the low latitude NmF2 is larger for the 27PCB simulation than for the simulations with daily varying LB perturbations (DPCB & DPDB) between doy 1 to 80 and doy 260 to 365, corresponding to approximately January to middle of March and middle of September to December.

The hmF2 does not exhibit significant differences in the magnitudes between the simulations indicating that the changes in NmF2 are not related to raising the plasma in a region of reduced recombination which would indicate that the equatorial vertical drift or equatorward winds are increased. The equatorial vertical drift in Figure 9 does not exhibit significant differences between the simulations and supports that the NmF2 changes are not caused by the vertical drift modifications.

To visualize this difference the mean NmF2 magnitude from (1) January, February, October-December and (2) June-August is presented in Figure 12. For the June-August mean the low latitude NmF2 is similar (at 16 LT, not shown here, the 3 simulations have almost the same low latitude NmF2 magnitude). In the October-February months the 27PCB NmF2 is consistently larger by approximately 50% in the low latitude region compared to the simulations with daily varying LB perturbation and background (DPDB). In both time periods the winter mid- and high latitude Nmf2 is up to 50% larger in the 27PCB simulation than in the DPDB simulations.

For 13 LT the longitudinal variation of NmF2 is depicted in Figure 13 for the selected time periods from Figure 10. The 3 simulations exhibit similar longitudinal variations with overall enhanced NmF2 magnitudes for the 27PCB case. For the 180-195 doy time period the longitudinal NmF2 variation for the 27PCB case is slightly modified with stronger peaks around $\pm 120^o$ longitude compared to the daily perturbation cases which may be related to the differences in the equatorial vertical drift during that time period (see Figure 10).

Liu et al. (2011) presented NmF2 and hmF2 variation for 2008-2009 derived from Constellation Observing System for Meteorology, Ionosphere and Climate (COSMIC) radio occultation measurements. They illustrated the seasonal latitudinal and longitudinal NmF2 and hmF2 variation at 13 LT. They found the largest low latitude NmF2 in March (defined as March equinox ±40 days) with peaks around 5.9 log10 $[1/cm^3]$ agreeing well with the 27PCB NmF2. *Burns et al.* (2012) analyzed COSMIC derived NmF2 and found that the second equinoctial peak occurs in October rather September which is reproduced by the 27DCB simulation however with a less pronounced peak as in the observations.

The longitudinal variation presented by *Liu et al.* (2011) for the different seasons is similar to the presented simulated longitudinal variation considering the shorter time periods (Figure 13) but there are differences between simulations and observations. Most notably the northern hemisphere has larger NmF2 in the 15-30 day period while during December solstice the southern hemisphere Nmf2 dominates over the northern hemisphere ones in the observations. The simulated annual asymmetry compares reasonably well with low latitude NmF values in June of around 5.6 log10 $[1/cm^3]$ (*Liu et al.*, 2011; *Burns et al.*, 2012). In the COSMIC NmF data a winter anomaly with higher values in the winter than summer hemisphere at conjugate points could not be identified (*Liu et al.*, 2011; *Burns et al.*, 2012). In contrast the 27PCB simulation exhibits a winter anomaly effect at low and mid latitudes.

This anomaly seems less pronounced in the simulations with daily varying LB (DPCB & DPDB), and it is weaker in the months of June-August. In the high latitude winter hemisphere local minima occur opposite to the winter anomaly. This effect was already pointed out by *Qian et al.* (2013) as a TIEGCM model-data discrepancy.
The hmF2 magnitude at low latitudes agrees reasonably well with the COSMIC hmF2 (*Liu et al.*, 2011). *Burns et al.* (2012) observes higher hmF2 around December than January which none of the simulations could reproduce. Note the presented hmF2 variations are for a particular longitude and local time while *Burns et al.* (2012) combined different local times and longitudes.

4.4 Global and diurnal mean total neutral density

A lot of interest is focused on modeling the neutral density at 400 km due to its importance for satellite drag determination. Several studies examined the global mean neutral density variations and illustrated the influence of the lower boundary on it (e.g., *Emmert et al.*, 2008; *Qian et al.*, 2009; *Siskind et al.*, 2014; *Lean et al.*, 2014; *Emmert*, 2015). In the TIEGCM-ICON we are not modifying the lower boundary eddy diffusivity K_{zz} according to *Qian et al.* (2009) to adjust the seasonal variation of the global mean neutral density since *Siskind et al.* (2014) pointed out that including the modified eddy diffusivity and increased tidal variability at the lower boundary leads to an underestimation of the F-region plasma density. Here, we rather state the influence of the different lower boundary options in perturbations and background on the global and diurnal mean density at 400 km for reference. For the conversion from pressure coordinates to the fixed altitude the geometric height was used.
The global and diurnal mean neutral density at 400 km for the three simulations is presented in Figure 14. Overall the simulations reveal similar seasonal variations. The bottom panel depicts the 30 day running mean to better visualize differences. The relative density difference between using climatological (DPCB) and daily varying (DPDB) LB background is between -2% during equinoxes, +3% in northern summer and up to +1% in northern winter with respect to the DPDB simulation. Using the 27 day average diurnal variation (27PCB) leads to a 4-5% increase in northern winter, 7-9% between doy 250-300, +4% in December and only +1.5% in northern summer. There is a consistent increase in the neutral density of the 27PCB case with respect to the DPDB & DPCB simulations.
The satellite drag derived neutral density (*Qian et al.*, 2013; *Emmert*, 2009) is in general lower than the simulated one in Figure 14. In the June-August months the observed density is as low as $0.3-0.4\times10^{-15}g/cm^3$. In October-November the density data peaks at $0.7\times10^{-15}g/cm^3$ and values around March equniox are between $0.5-0.55\times10^{-15}g/cm^3$. This leads to the largest difference in June-August (around $0.15-0.25\times10^{-15}g/cm^3$) and smallest in October-November with approximately $0.05\times10^{-15}g/cm^3$.

5 Discussion

In the following the persistent differences between the three simulations will be discussed in more detail. In the previous section it was illustrated that employing the 27 day averaged diurnal variation (27PCB) as LB perturbations leads to higher NmF2, approximately 50% larger at low latitudes and in the winter middle to high latitude region compared to forcing with daily varying LB perturbations (DPCB & DPDB).
The 27PCB simulation compared to the DPCB simulation includes less tidal variability at

the lower boundary (shown for neutral temperature in Figure 4). Several studies have pointed out that increases in tidal activity at the model lower boundary leads to a decrease in NmF2 due to changes in the neutral composition (e.g., *Forbes et al.*, 1993; *Yamazaki and Richmond*, 2013; *Siskind et al.*, 2014; *Jones et al.*, 2014).

Some of these studies analyzed TIEGCM simulations to identify possible mechanisms. *Yamazaki and Richmond* (2013) examined equinox TIEGCM simulations with and without migrating tidal forcing at the LB. Including the migrating tides at the LB lead to a 15% decrease in total electron content (TEC) and a 20-30% reduction in O/N2 mixing ratio at F-region heights. *Siskind et al.* (2014) performed year long TIEGCM simulations with tidal components defined by climatology (low tidal variability) and the Navy Operational Global Atmospheric Prediction System (NOGAPS), ALPHA (Advanced Level Physics High Altitude) forecast model (large tidal variability). In addition they varied the vertical eddy diffusion coefficient (K_{zz}) at the LB according to *Qian et al.* (2009). They found that the increases in tidal variability and eddy diffusivity acts in a similar way by reducing the O/N2 mixing ratio and decreasing the F-region plasma. Similar results were found by *Jones et al.* (2014) based on the comparison of year long TIEGCM simulations with and without tidal LB perturbations.

The studies differ in the proposed mechanisms causing the reduction in O/N2 ratio with increased tidal activity. *Akmaev and Shved* (1980) and *Forbes et al.* (1993) proposed that the tides lead to an O decrease through an increase in the three-body recombination. However, *Yamazaki and Richmond* (2013) found that this mechanism is not very effective above 96 km for the upward propagating diurnal tides. Instead they proposed that the dissipating tides in the lower thermosphere change the mean meridional circulation leading to upward equatorial winds and downward high latitude winds which causes a net upward transport of O at low latitude and a downward transport of O and therefore loss of O at high latitude. *Jones et al.* (2014) suggested that a net vertical flux of the constituents plays a role which was termed “dynamical transport”. We refer to these studies and references therein for a detailed discussion.

In Figure 15 the zonal and diurnal mean mass mixing ratio of O/N2 is depicted. The variation at Z=2.875 (approximately 300 km) and Z=-4.125 (approximately 120 km) are shown on the left and right, respectively, for the 27PCB, DPCB, and DPDB simulation from top to bottom. The increase in the O/N2 mass mixing ratio in the case of 27PCB is consistent with the findings of e.g., *Yamazaki and Richmond* (2013); *Siskind et al.* (2014); *Jones et al.* (2014) that an increase in tidal activity at the LB decreases the O/N2 ratio. Figure 17 depicts the height variation of the relative O and N2 number density change of the 27PCB case with respect to the DPCB simulation illustrating that the modification in composition is already happening in the lower thermosphere close to the lower boundary.

In Figure 16 the monthly mean O/N2 variation in the F-region (Z=2.875) is depicted corresponding to the mean NmF2 at 13 LT in Figure 12. There is a strong correlation between the increase in O/N2 and the increase in NmF2 in the 27PCB case compared to the DPDB case. This suggests that the changes in the O/N2 ratio are at least in part responsible for the increase in NmF2 in the 27PCB case. At low latitudes the O/N2 ratio increase for the 27PCB case is larger in the months of October through February than for the months of June to August which agrees with the larger enhancement in NmF2 during the October through February months compared to June to August for the 27PCB simulation.

Comparing 27PCB O/N2 and NmF2 with the ones from DPCB (Figure 16 and Figure 12, respectively) a hemispheric asymmetry can be identified with large enhancements in the winter hemisphere but no or very small changes in the summer hemisphere. To our knowledge none of the above mentioned studies identified a hemispheric asymmetry in the O/N2 ratio. The causes of this hemispheric asymmetry is not in the purview of this study and will be addressed in a separate study.

The other persistent change of the 27PCB simulation compared to the DPCB case is the increase in the neutral density presented in Figure 14. The presented changes are at a constant altitude and not a constant pressure level. To examine this increase in more detail we focus on a representative time frame between doy 43 to 73 and the time averaged global mean height variation. The top panel in Figure 17 illustrates the global mean, time averaged total neutral density change of the 27PCB case with respect to the DPCB simulation. The density first decreases up to approximately 180 km and then increases compared to the case with more tidal variability at the LB.

The global mean, time averaged neutral temperature is decreased at all heights in the case with less tidal variability (27PCB) compared to the DPCB case (see Figure 17 middle panel). The temperature difference is increasing up to approximately 200 km and remains negative above. A temperature decrease will lead to a smaller scale height and a faster decrease in the O and N2 density with altitude compared to the DPCB case, and therefore leads to a neutral density reduction if the composition is not changing. The composition differences are illustrated in the bottom panel of Figure 17 by the relative changes in O and N2 number density of the 27PCB case with respect to the DPCB case. Up to approximately 190 km N2 number density is larger than the O number density (not depicted). This suggests that the decrease in N2 dominates over the increase in O in the lower thermosphere and leads to a decrease in total density. Once the composition is dominated by O the total neutral density is increasing compared to the DPCB case. The steady decrease of the relative number density change in O and N2 above approximately 140 km may be related to the decrease in the neutral temperature and the reduced scale height.

6 Summary

In this study the TIEGCM-ICON was introduced and the specific features were highlighted. The important change is in the lower boundary forcing of the model with a seasonal and latitudinal varying background and daily varying, 27-day averaged diurnal tidal perturbations. In this study we present results from the TIEGCM-ICON and examine the behavior due to the lower boundary changes specifically due to the 27-day averaged diurnal variation. This will provide some guidance for the interpretation of the simulation results accompanying the ICON mission. The presented results are for the year 2009. The solar radiation in 2009 might be lower than what is expected in the upcoming solar minimum into which ICON will be launched.

We focused on the neutral temperature tidal components and the comparison between the simulations and published results (e.g., *Häusler et al.*, 2015). These comparisons indicated that the latitudinal and seasonal features could be reproduced by the simulations (27PCB, DPCB, DPDB) in the E- and F-region. Similarly the equatorial vertical ExB drift compares reasonably with C/NOFS observations (*Stoneback et al.*, 2013). The main difference is that in general the simulated daytime vertical drift is weaker than the observed one.

The peak of the F-region plasma density NmF2 is consistently larger for the simulation with 27 day averaged diurnal LB variation (27PCB) compared to the daily varying LB variations (DPCB, DPDB). The height of the peak (hmF2) does not exhibit major changes between the simulations. The O/N2 ratio is enhanced for the case of 27PCB compared to the other two cases. This agrees with findings from e.g., *Akmaev and Shved* (1980); *Forbes et al.* (1993); *Yamazaki and Richmond* (2013); *Siskind et al.* (2014); *Jones et al.* (2014) that increasing the tidal activity in the upper mesosphere / lower thermosphere is decreasing the O/N2 ratio. This reduction is then propagated into the F-region through molecular diffusion.

The changes in NmF2 due to the decrease in LB tidal variability can be up to 50% in the low latitude region and in the winter high latitude region in the months of January, February and October to December. The hemispheric asymmetry in the NmF2 and O/N2 changes of the 27PCB case with respect to the DPCB & DPDB cases are not addressed in this study. Overall the NmF2 and hmF2 of the 27PCB compares well in magnitude with published COSMIC observations (e.g., *Liu et al.*, 2011; *Burns et al.*, 2012).

The total neutral density at 400 km experiences an increase if the LB tidal activity is reduced (27PCB). Closer examination reveal that the total neutral density of the 27PCB case is first decreasing up to approximately 180 km before increasing relative to the DPCB case. Diagnostics of N2 and O number density height variations illustrate that there is a relative decrease in N2 density (27PCB relative to DPCB) and an relative increase in O over all heights. The reduction in N2 density can explain the decrease of the total density in the region dominated by N2. Closer to the transition region of O becoming the dominant species the relative total neutral density is increasing.

The TIEGCM-ICON will provide simulation results during the ICON mission. The major quantities will be saved e.g., neutral wind, composition, temperature, plasma distribution and temperature, ExB drift, electric fields and used to study the vertical coupling mechanisms.

Acknowledgements A.M. would like to thank A.D. Richmond for comments on an earlier draft. A.M. was supported by NASA grant NNX14AP03G. The National Center for Atmospheric Research is sponsored by the National Science Foundation. ICON is supported by NASAs Explorers Program through contracts NNG12FA45C and NNG12FA42I. We would like to acknowledge high-performance computing support from Yellowstone (ark:/85065/d7wd3xhc) provided by NCAR's Computational and Information Systems Laboratory, sponsored by the National Science Foundation. The National Center for Atmospheric Research is sponsored by the National Science Foundation. The author would like to thank the reviewers for their helpful comments.

References

Akmaev, R. A., and G. M. Shved (1980), Modelling of the composition of the lower thermosphere taking account of the dynamics with applications to tidal variations of the forbidden O I 5577 A airglow, *Journal of Atmospheric and Terrestrial Physics*, *42*, 705–716.

Alken, P., A. Chulliat, and S. Maus (2013), Longitudinal and seasonal structure of the ionospheric equatorial electric field, *Journal of Geophysical Research: Space Physics*, *118*(3), 1298–1305, doi:10.1029/2012JA018314.

Burns, A. G., S. C. Solomon, W. Wang, L. Qian, Y. Zhang, and L. J. Paxton (2012), Daytime climatology of ionospheric NmF2 and hmF2 from COSMIC data, *Journal of Geophysical Research: Space Physics*, *117*(A9), doi:10.1029/2012JA017529, a09315.

Dickinson, R. E., E. Ridley, and R. Roble (1984), Thermospheric general circulation with coupled dynamics and composition, *Journal of the Atmospheric Sciences*, *41*(2), 205–219.

Drob, D. P., et al. (2008), An empirical model of the earth's horizontal wind fields: Hwm07, *Journal of Geophysical Research: Space Physics*, *113*(A12), doi:10.1029/2008JA013668, a12304.

Drob, D. P., et al. (2015), An update to the horizontal wind model (HWM): The quiet time thermosphere, *Earth and Space Science*, *2*(7), 301–319, doi:10.1002/2014EA000089.

Emery, B., R. Roble, E. Ridley, A. Richmond, D. Knipp, G. Crowley, D. Evans, F. Rich, and S. Maeda (2012), Parameterization of the ion convection and the auroral oval in the NCAR Thermospheric General Circulation Models, *Tech. rep.*, National Center for Atmospheric Research, Boulder CO, USA, doi:10.5065/D6N29TXZ.

Emmert, J. (2009), A long-term data set of globally averaged thermospheric total mass density, *Journal of Geophysical Research: Space Physics*, *114*(A6).

Emmert, J. (2015), Thermospheric mass density: A review, *Advances in Space Research*, *56*(5), 773 – 824, doi:http://dx.doi.org/10.1016/j.asr.2015.05.038.

Emmert, J. T., J. M. Picone, and R. R. Meier (2008), Thermospheric global average density trends, 1967-2007, derived from orbits of 5000 near-Earth objects, *Geophysical Research Letters*, *35*(5), doi:10.1029/2007GL032809, l05101.

England, S. L., T. J. Immel, J. D. Huba, M. E. Hagan, A. Maute, and R. DeMajistre (2010), Modeling of multiple effects of atmospheric tides on the ionosphere: An examination of possible coupling mechanisms responsible for the longitudinal structure of the equatorial ionosphere, *J. Geophys. Res.*, *115*(A5), doi:10.1029/2009JA014894.

Fang, T., A. Richmond, J. Liu, A. Maute, C. Lin, C. Chen, and B. Harper (2008), Model simulation of the equatorial electrojet in the Peruvian and Philippine sectors, *J. Atmos. Sol.-Terr. Phys.*, *70*(17), 2203 – 2211, doi:http://dx.doi.org/10.1016/j.jastp.2008.04.021.

Fejer, B. G., J. W. Jensen, and S.-Y. Su (2008), Quiet time equatorial F region vertical plasma drift model derived from ROCSAT-1 observations, *J. Geophys. Res.*, *113*(A5), doi:10.1029/2007JA012801.

Forbes, J. M., and M. E. Hagan (1982), Thermospheric extensions of the classical expansion functions for semidiurnal tides, *Journal of Geophysical Research: Space Physics*, *87*(A7), 5253–5259, doi:10.1029/JA087iA07p05253.

Forbes, J. M., R. G. Roble, and C. G. Fesen (1993), Acceleration, heating, and compositional mixing of the thermosphere due to upward propagating tides, *Journal of Geophysical Research: Space Physics*, *98*(A1), 311–321, doi:10.1029/92JA00442.

Häusler, K., and H. Lühr (2009), Nonmigrating tidal signals in the upper thermospheric zonal wind at equatorial latitudes as observed by CHAMP, *Ann. Geophys*, *27*(7), 2643–2652.

Häusler, K., H. Lühr, M. E. Hagan, A. Maute, and R. G. Roble (2010), Comparison of CHAMP and TIME-GCM nonmigrating tidal signals in the thermospheric zonal wind, *J. Geophys. Res.: Atmospheres*, *115*(D1), doi:10.1029/2009JD012394.

Häusler, K., M. E. Hagan, J. M. Forbes, X. Zhang, E. Doornbos, S. Bruinsma, and G. Lu (2015), Intraannual variability of tides in the thermosphere from model simulations and in situ satellite observations, *Journal of Geophysical Research: Space Physics*, *120*(1), 751–765, doi:10.1002/2014JA020579, 2014JA020579.

Heelis, R. A., J. K. Lowell, and R. W. Spiro (1982), A model of the high-latitude ionospheric convection pattern, *J. Geophys. Res.*, *87*(A8), 6339–6345, doi:10.1029/JA087iA08p06339.

Hui, D., and B. G. Fejer (2015), Daytime plasma drifts in the equatorial lower ionosphere, *Journal of Geophysical Research: Space Physics*, *120*(11), 9738–9747, doi:10.1002/2015JA021838, 2015JA021838.

Immel, T. J., E. Sagawa, S. L. England, S. B. Henderson, M. E. Hagan, S. B. Mende, H. U. Frey, C. M. Swenson, and L. J. Paxton (2006), Control of equatorial ionospheric morphology by atmospheric tides, *Geophysical Research Letters*, *33*(15), doi:10.1029/2006GL026161.

Jin, H., Y. Miyoshi, H. Fujiwara, H. Shinagawa, K. Terada, N. Terada, M. Ishii, Y. Otsuka, and A. Saito (2011), Vertical connection from the tropospheric activities to the ionospheric longitudinal structure simulated by a new Earth's whole atmosphere-ionosphere coupled model, *J. Geophys. Res.*, *116*(A1), doi:10.1029/2010JA015925, a01316.

Jones, M., J. M. Forbes, M. E. Hagan, and A. Maute (2014), Impacts of vertically propagating tides on the mean state of the ionosphere-thermosphere system, *Journal of Geophysical Research: Space Physics*, *119*(3), 2197–2213, doi:10.1002/2013JA019744.

Jones, M., J. M. Forbes, and M. E. Hagan (2016), Solar cycle variability in mean thermospheric composition and temperature induced by atmospheric tides, *Journal of Geophysical Research: Space Physics*, *121*(6), 5837–5855, doi:10.1002/2016JA022701, 2016JA022701.

Kil, H., and L. J. Paxton (2011), The origin of the nonmigrating tidal structure in the column number density ratio of atomic oxygen to molecular nitrogen, *Geophysical Research Letters*, *38*(19), doi:10.1029/2011GL049432, l19108.

Kil, H., S.-J. Oh, M. C. Kelley, L. J. Paxton, S. L. England, E. Talaat, K.-W. Min, and S.-Y. Su (2007), Longitudinal structure of the vertical ExB drift and ion density seen from ROCSAT-1, *Geophysical Research Letters*, *34*(14), doi:10.1029/2007GL030018.

Le Mouël, J.-L., P. Shebalin, and A. Chulliat (2006), The field of the equatorial electrojet from CHAMP data, *Annales Geophysicae*, *24*(2), 515–527, doi:10.5194/angeo-24-515-2006.

Lean, J. L., S. E. McDonald, J. D. Huba, J. T. Emmert, D. P. Drob, and C. L. Siefring (2014), Geospace variability during the 2008-2009 whole heliosphere intervals, *Journal of Geophysical Research: Space Physics*, *119*(5), 3755–3776, doi:10.1002/2013JA019485.

Lin, C. H., C. C. Hsiao, J. Y. Liu, and C. H. Liu (2007), Longitudinal structure of the equatorial ionosphere: Time evolution of the four-peaked EIA structure, *J. Geophys. Res.*, *112*(A12), doi:10.1029/2007JA012455.

Liu, H., and S. Watanabe (2008), Seasonal variation of the longitudinal structure of the equatorial ionosphere: Does it reflect tidal influences from below?, *Journal of Geophysical Research: Space Physics*, *113*(A8), doi:10.1029/2008JA013027.

Liu, H., M. Yamamoto, and H. Lhr (2009), Wave-4 pattern of the equatorial mass density anomaly: A thermospheric signature of tropical deep convection, *Geophysical Research Letters*, *36*(18), doi:10.1029/2009GL039865.

Liu, H., H. Jin, Y. Miyoshi, H. Fujiwara, and H. Shinagawa (2013), Upper atmosphere response to stratosphere sudden warming: Local time and height dependence simulated by GAIA model, *Geophysical Research Letters*, *40*(3), 635–640, doi:10.1002/Geophys. Res. Letters.50146.

Liu, L., H. Le, Y. Chen, M. He, W. Wan, and X. Yue (2011), Features of the middle- and low-latitude ionosphere during solar minimum as revealed from cosmic radio occultation measurements, *Journal of Geophysical Research: Space Physics*, *116*(A9), doi: 10.1029/2011JA016691.

Lühr, H., S. Maus, and M. Rother (2004), Noon-time equatorial electrojet: Its spatial features as determined by the champ satellite, *Journal of Geophysical Research: Space Physics*, *109*(A1), doi:10.1029/2002JA009656.

Maute, A., A. D. Richmond, and R. G. Roble (2012), Sources of low-latitude ionospheric ExB drifts and their variability, *J. Geophys. Res.*, *117*(A6), doi:10.1029/2011JA017502.

Oberheide, J., J. M. Forbes, X. Zhang, and S. L. Bruinsma (2011a), Wave-driven variability in the ionosphere-thermosphere-mesosphere system from TIMED observations: What contributes to the "wave 4"?, *J. Geophys. Res.*, *116*(A1), doi:10.1029/2010JA015911.

Oberheide, J., J. M. Forbes, X. Zhang, and S. L. Bruinsma (2011b), Climatology of upward propagating diurnal and semidiurnal tides in the thermosphere, *J. Geophys. Res.*, *116*(A11), doi:10.1029/2011JA016784.

Pedatella, N. M., and A. Maute (2015), Impact of the semidiurnal lunar tide on the midlatitude thermospheric wind and ionosphere during sudden stratosphere warmings, *Journal of Geophysical Research: Space Physics*, *120*(12), 10,740–10,753, doi: 10.1002/2015JA021986, 2015JA021986.

Pedatella, N. M., A. D. Richmond, A. Maute, and H.-L. Liu (2016), Impact of semidiurnal tidal variability during ssws on the mean state of the ionosphere and thermosphere, *Journal of Geophysical Research: Space Physics*, doi:10.1002/2016JA022910.

Picone, J. M., A. E. Hedin, D. P. Drob, and A. C. Aikin (2002), Nrlmsise-00 empirical model of the atmosphere: Statistical comparisons and scientific issues, *Journal of Geophysical Research: Space Physics*, *107*(A12), doi:10.1029/2002JA009430.

Qian, L., S. C. Solomon, and T. J. Kane (2009), Seasonal variation of thermospheric density and composition, *Journal of Geophysical Research: Space Physics*, *114*(A1), doi: 10.1029/2008JA013643.

Qian, L., A. G. Burns, S. C. Solomon, and W. Wang (2013), Annual/semiannual variation of the ionosphere, *Geophysical Research Letters*, *40*(10), 1928–1933, doi: 10.1002/grl.50448.

Qian, L., et al. (2014), The NCAR TIE-GCM: A community model of the coupled thermosphere/ionosphere system, *Modeling the Ionosphere-Thermosphere System, Geophys. Monogr. Ser*, *201*, 73–83.

Richards, P., J. Fennelly, and D. Torr (1994), EUVAC: A solar EUV flux model for aeronomic calculations, *J. Geophys. Res.*, *99*, 8981–1992.

Richmond, A. (1995), Ionospheric electrodynamics, in *Handbook of atmospheric electrodynamics, Vol. II*, edited by H. Volland, pp. 249–290, CRC Press, Inc.

Richmond, A., and A. Maute (2013), Ionospheric electrodynamics modeling, in *Modeling the Ionosphere-Thermosphere*, vol. 201, edited by R. S. J.D. Huba and G. Khazanov, pp. (also published online in 2014 by John Wiley & Sons, Ltd, Chichester, UK. doi:10.1002/9781118704,417.ch6), AGU Geophysical Monograph Series., doi: 10.1029/2012GM001331.

Richmond, A. D., E. C. Ridley, and R. G. Roble (1992), A thermosphere/ionosphere general circulation model with coupled electrodynamics, *Geophysical Research Letters*, *19*(6), 601–604, doi:10.1029/92GL00401.

Roble, R., and E. Ridley (1987), An auroral model for the NCAR thermospheric general circulation model (TGCM), *Ann. Geophys.*, *5A*, 369–382.

Roble, R., E. Ridley, and A. Richmond (1988), A coupled thermosphere / ionosphere general circulation model, *Geophys. Res. Letters*, *15*, 1325–1328.

Siskind, D. E., D. P. Drob, K. F. Dymond, and J. P. McCormack (2014), Simulations of the effects of vertical transport on the thermosphere and ionosphere using two coupled models, *J. Geophys. Res.*, *119*(2), 1172–1185, doi:10.1002/2013JA019116.

Solomon, S. C., A. G. Burns, B. A. Emery, M. G. Mlynczak, L. Qian, W. Wang, D. R. Weimer, and M. Wiltberger (2012), Modeling studies of the impact of high-speed streams and co-rotating interaction regions on the thermosphere-ionosphere, *Journal of Geophysical Research: Space Physics*, *117*(A9), doi:10.1029/2011JA017417.

Stoneback, R., R. Heelis, A. Burrell, W. Coley, B. G. Fejer, and E. Pacheco (2011), Observations of quiet time vertical ion drift in the equatorial ionosphere during the solar minimum period of 2009, *J. Geophys. Res.*, *116*(A12).

Stoneback, R. A., N. K. Malakar, D. J. Lary, and R. A. Heelis (2013), Specifying the equatorial ionosphere using cindi on c/nofs, cosmic, and data interpolating empirical orthogonal functions, *Journal of Geophysical Research: Space Physics*, *118*(10), 6706–6722, doi: 10.1002/jgra.50596.

Sutton, E. K., J. P. Thayer, W. Wang, S. C. Solomon, X. Liu, and B. T. Foster (2015), A self-consistent model of helium in the thermosphere, *Journal of Geophysical Research: Space Physics*, *120*(8), 6884–6900, doi:10.1002/2015JA021223, 2015JA021223.

Thébault, E., et al. (2015), International geomagnetic reference field: the 12th generation, *Earth, Planets and Space*, *67*(1), 1–19.

Weimer, D. R. (2005), Improved ionospheric electrodynamic models and application to calculating joule heating rates, *J. Geophys. Res.*, *110*(A5), doi:10.1029/2004JA010884.

Yamazaki, Y., and A. D. Richmond (2013), A theory of ionospheric response to upward-propagating tides: Electrodynamic effects and tidal mixing effects, *J. Geophys. Res.*, *118*(9), 5891–5905, doi:10.1002/jgra.50487.

Yamazaki, Y., et al. (2014), Ground magnetic effects of the equatorial electrojet simulated by the tie-gcm driven by timed satellite data, *Journal of Geophysical Research: Space Physics*, *119*(4), 3150–3161, doi:10.1002/2013JA019487.

Zhang, Y., S. England, and L. J. Paxton (2010), Thermospheric composition variations due to nonmigrating tides and their effect on ionosphere, *Geophysical Research Letters*, *37*(17), doi:10.1029/2010GL044313, l17103.

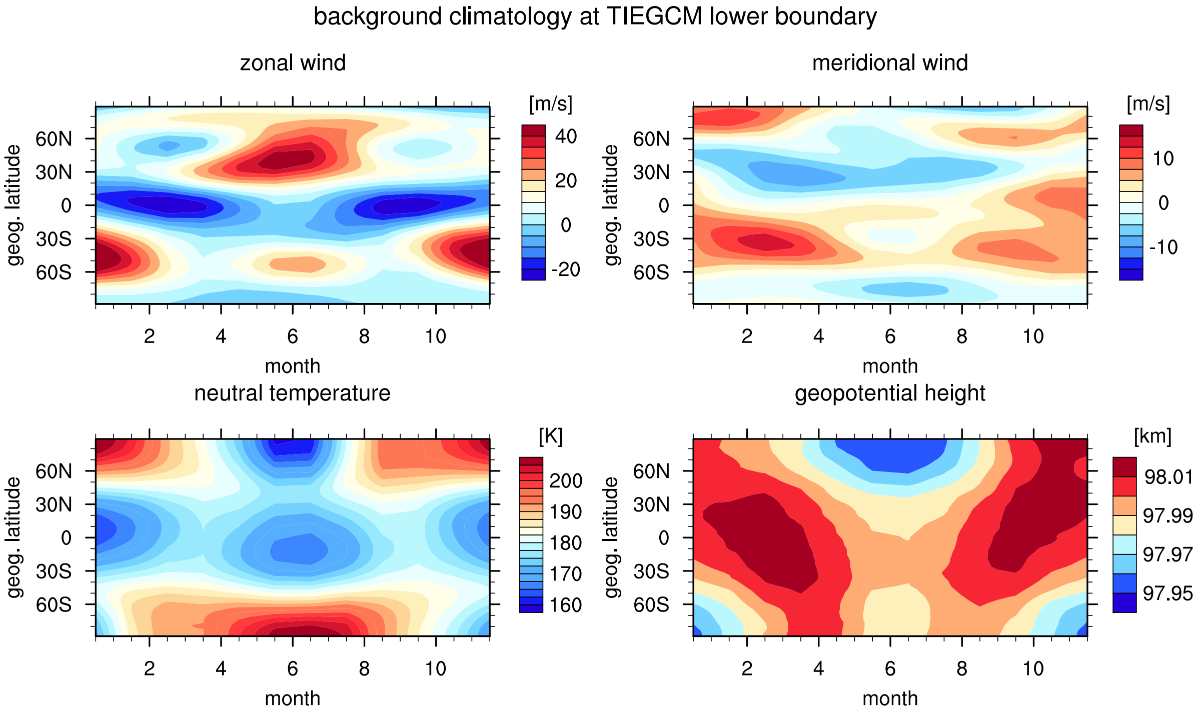

Fig. 1 Monthly background climatology based on HWM07 and MSISE00 for the TIEGCM lower boundary. The values for middle of January are depicted at month index 0.5, for February at month index 1.5 and so on.

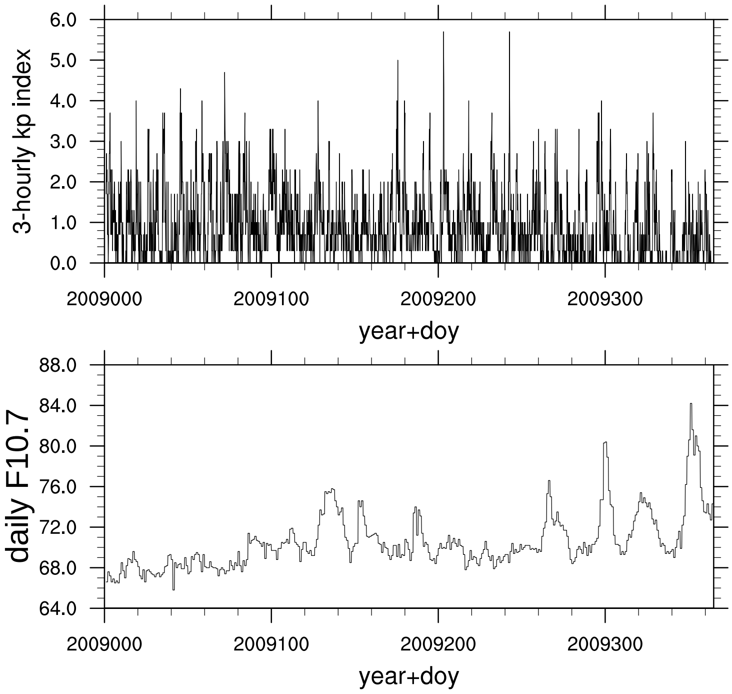

Fig. 2 Geophysical conditions for 2009: 3-hourly Kp index (top), and daily $F_{10.7}$ solar flux (bottom).

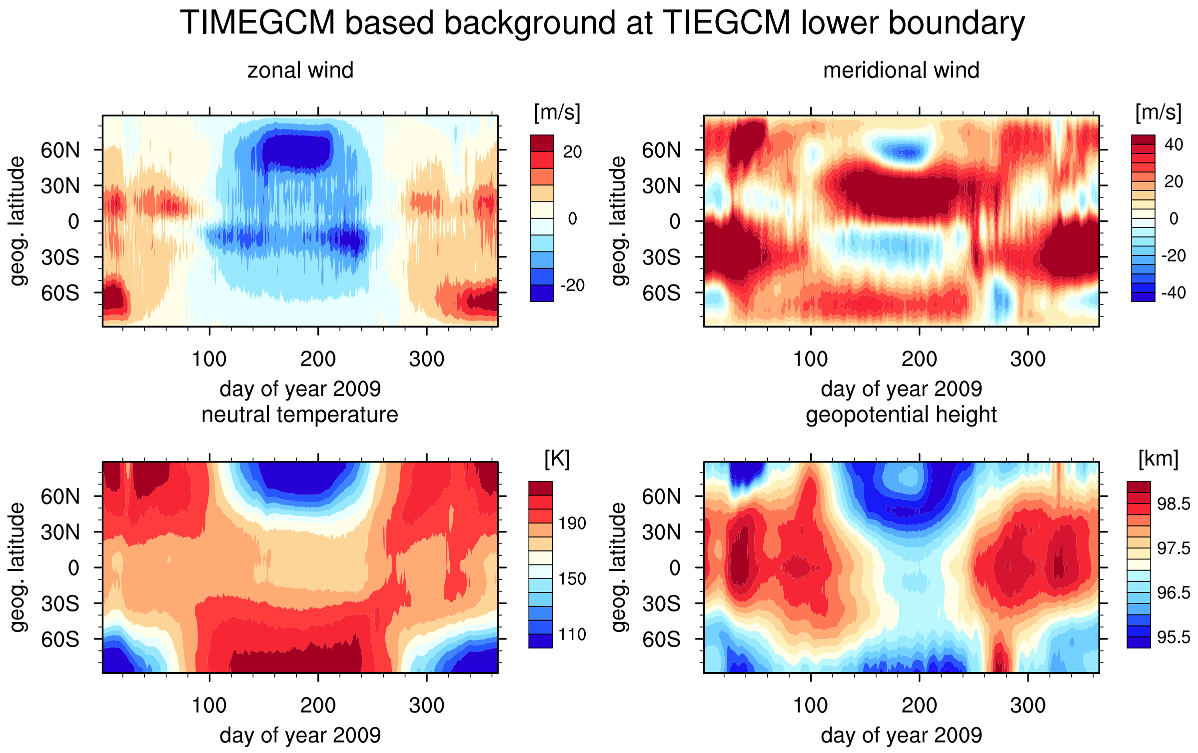

Fig. 3 Daily varying background based on TIMEGCM 2009 simulation (*Häusler et al.*, 2015). The TIMEGCM quantities are interpolated to Z=-7 pressure level and the diurnal and zonal mean taken.

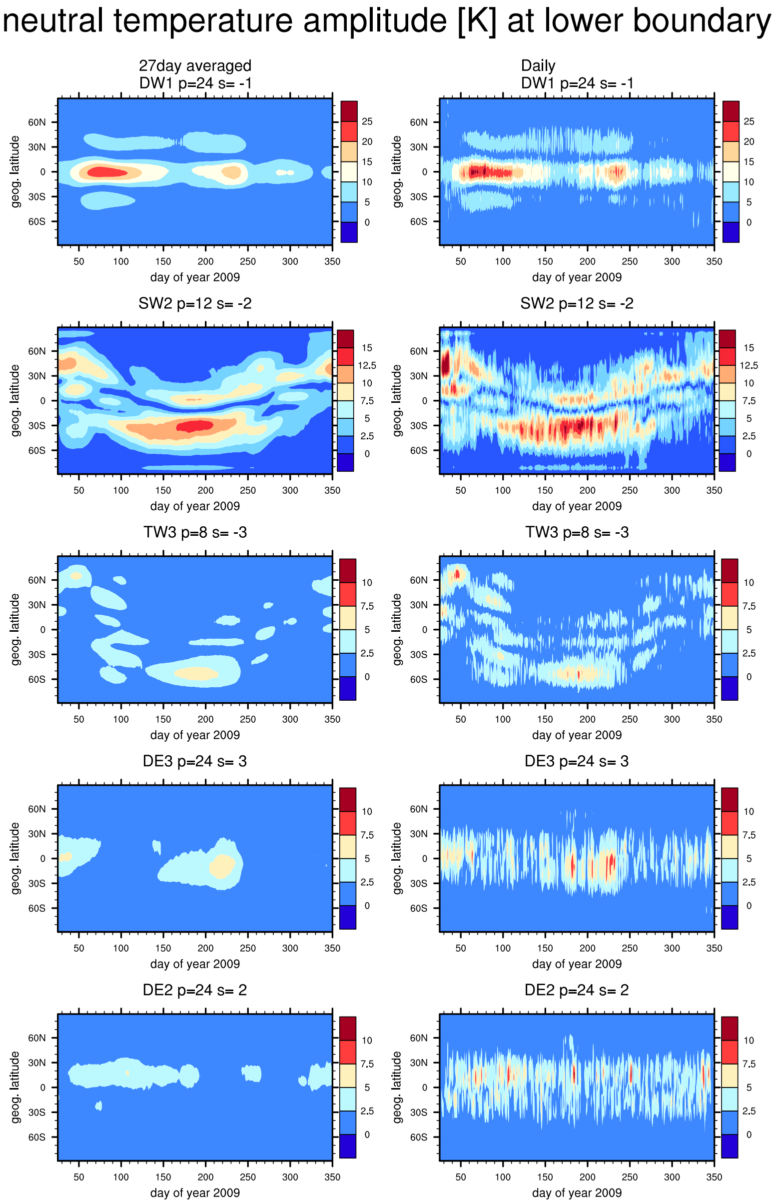

Fig. 4 Neutral temperature amplitude [K] at the lower boundary of TIEGCM-ICON based on the 27-day averaged diurnal TIMEGCM variation (left), and based on daily diurnal TIMEGCM variation (right).

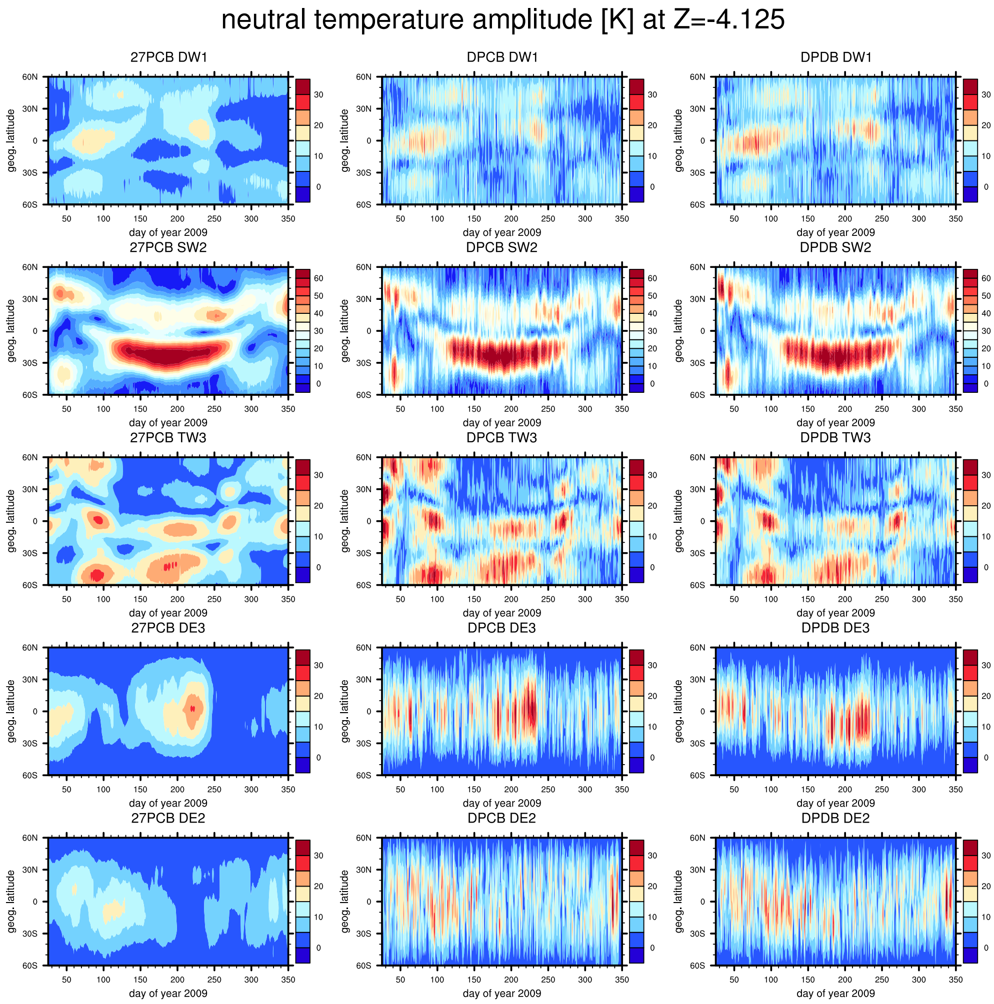

Fig. 5 Neutral temperature amplitude at Z=-4.125 (approximately 120 km) for DW1, SW2, TW3, DE3, and DE2 based a daily processing window for the simulations: 27 day averaged TIMEGCM diurnal perturbation and climatological background (left, 27PCB), daily TIMEGCM perturbation and climatological background (middle, DPCB), and daily TIMEGCM perturbations and background (right, DPDB).

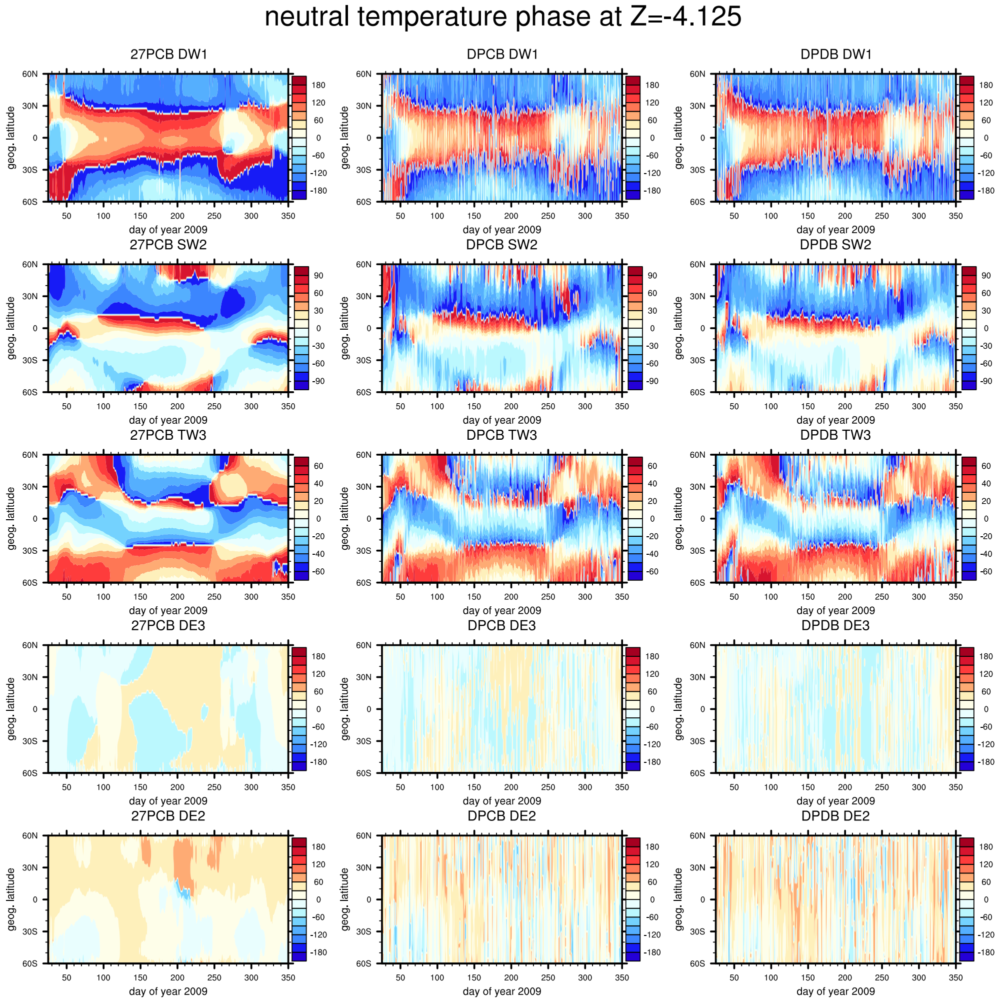

Fig. 6 Neutral temperature phase at Z=-4.125 (approximately 120 km) for DW1, SW2, TW3, DE3, and DE2 based a daily processing window for the simulations: 27 day averaged TIMEGCM diurnal perturbation and climatological background (left, 27PCB), daily TIMEGCM perturbation and climatological background (middle, DPCB), and daily TIMEGCM perturbations and background (right, DPDB). Phase is defined as the longitude of the maximum at 0UT.

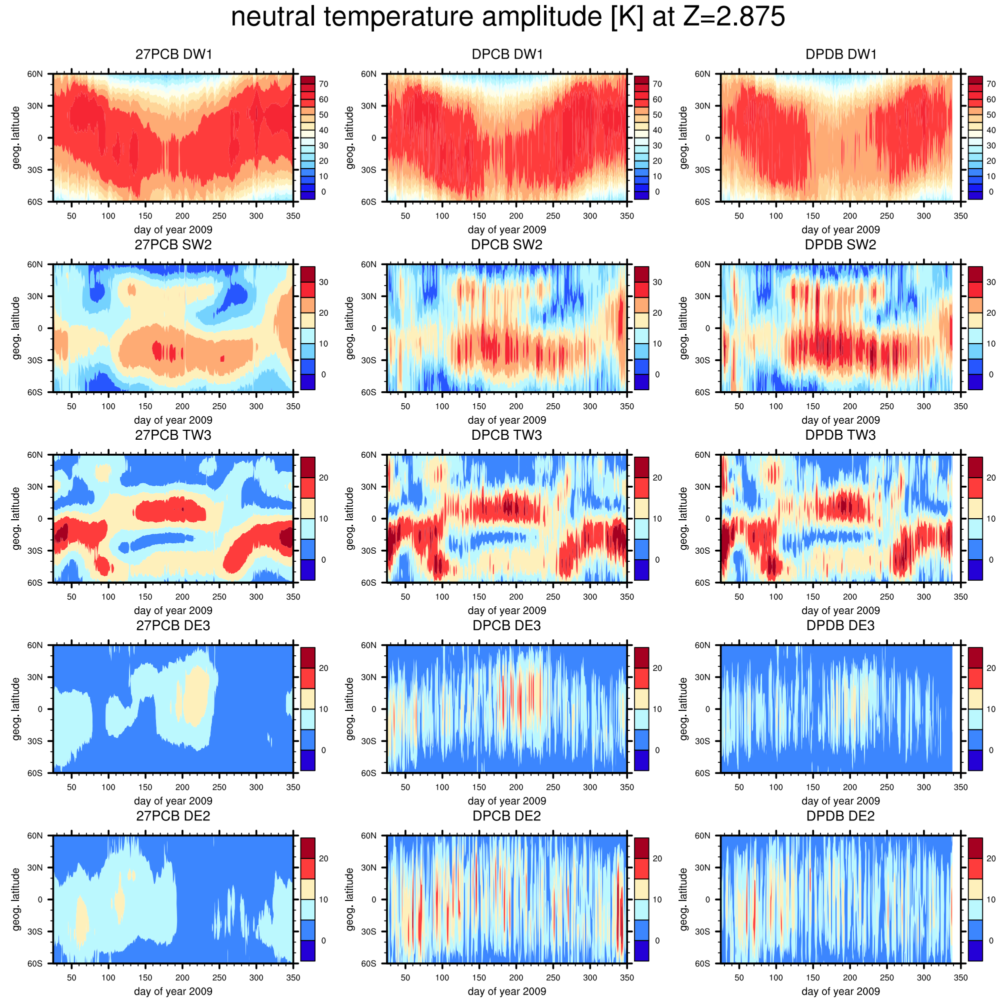

Fig. 7 Neutral temperature amplitude at Z=2.875 (approximately 300 km) for DW1, SW2, TW3, DE3, and DE2 based a daily processing window for the simulations: 27 day averaged TIMEGCM diurnal perturbation and climatological background (left, 27PCB), daily TIMEGCM perturbation and climatological background (middle, DPCB), and daily TIMEGCM perturbations and background (right, DPDB).

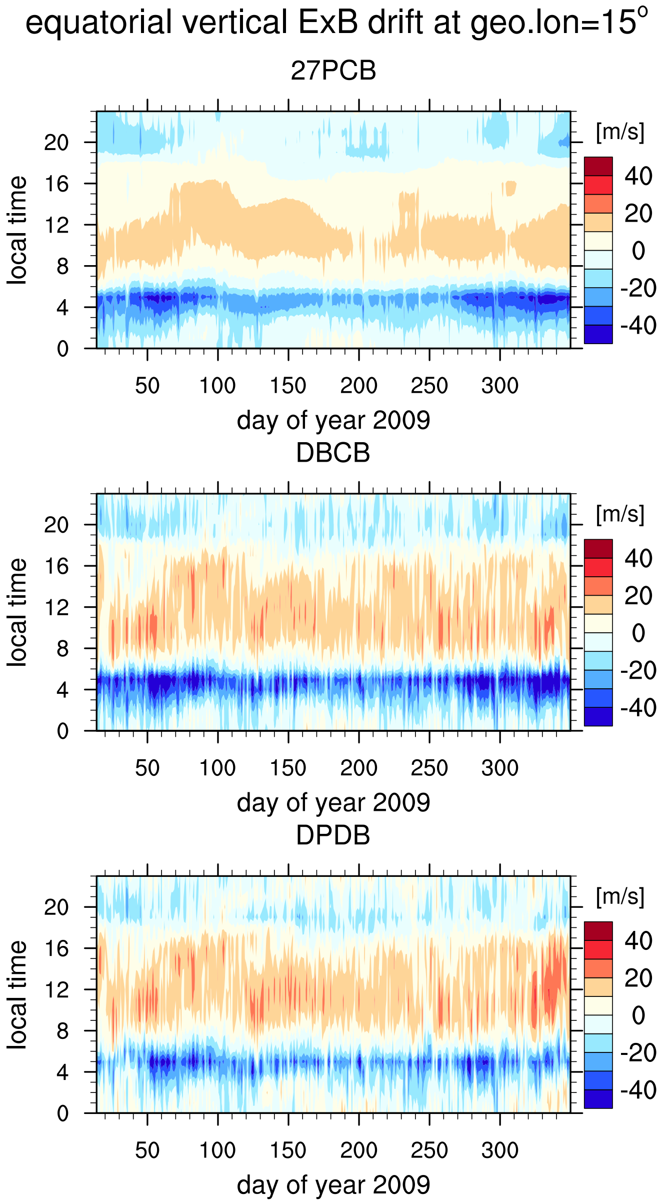

Fig. 8 Local time variation of the vertical ExB drift [m/s] at magnetic equator (geographic latitude $\lambda = 11^o$, geographic longitude $\phi = 15^o$, pressure level Z=2) for 2009 simulations: 27 day averaged TIMEGCM diurnal perturbation and climatological background (top, 27PCB); daily TIMEGCM perturbation and climatological background (middle, DPCB); daily TIMEGCM perturbations and background (bottom, DPDB).

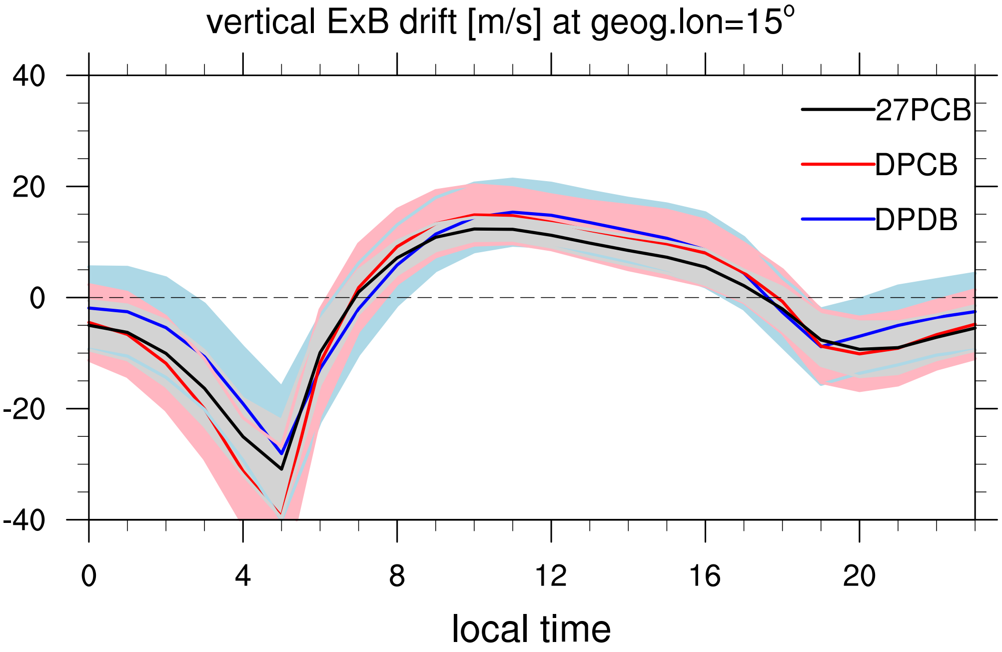

Fig. 9 Diurnal variation of mean vertical ExB drift [m/s] (lines) and standard deviation (colored filled) at geographic latitude $\lambda = 11^o$, geographic longitude $\phi = 15^o$, pressure level Z=2) for 2009 simulations: daily TIMEGCM perturbations and background (blue, DPDB); daily TIMEGCM perturbation and climatological background (red, DPCB), 27 day averaged TIMEGCM diurnal perturbation and climatological background (black, 27PCB).

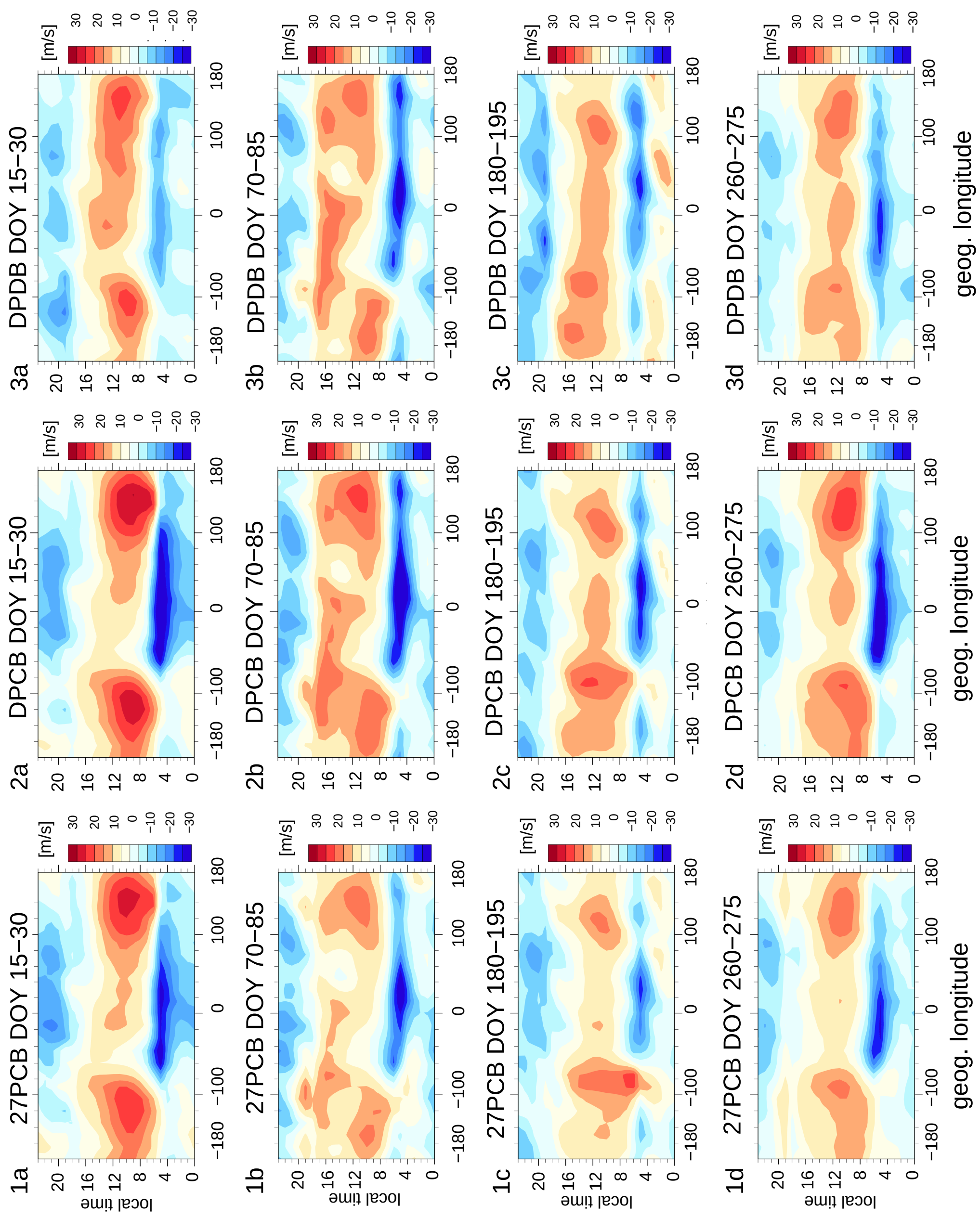

Fig. 10 Local time and geographic longitude variation of vertical ExB drift [m/s] at the magnetic equator for the 2009 simulations: 27 day averaged TIMEGCM diurnal perturbation and climatological background (1a-1d, left panels, 27PCB); daily TIMEGCM perturbation and climatological background (2a-2d; middle panels, DPCB); daily TIMEGCM perturbations and background (3a-3d, right panels, DPDB). The depicted variations are an 15-day average from day of year (doy) 15-30 (1a, 2a, 3a), doy 70-85 (1b, 2b,3b), doy 180-195 (1c,2c,3c), and doy 260-275 (1d, 2d, 3d).

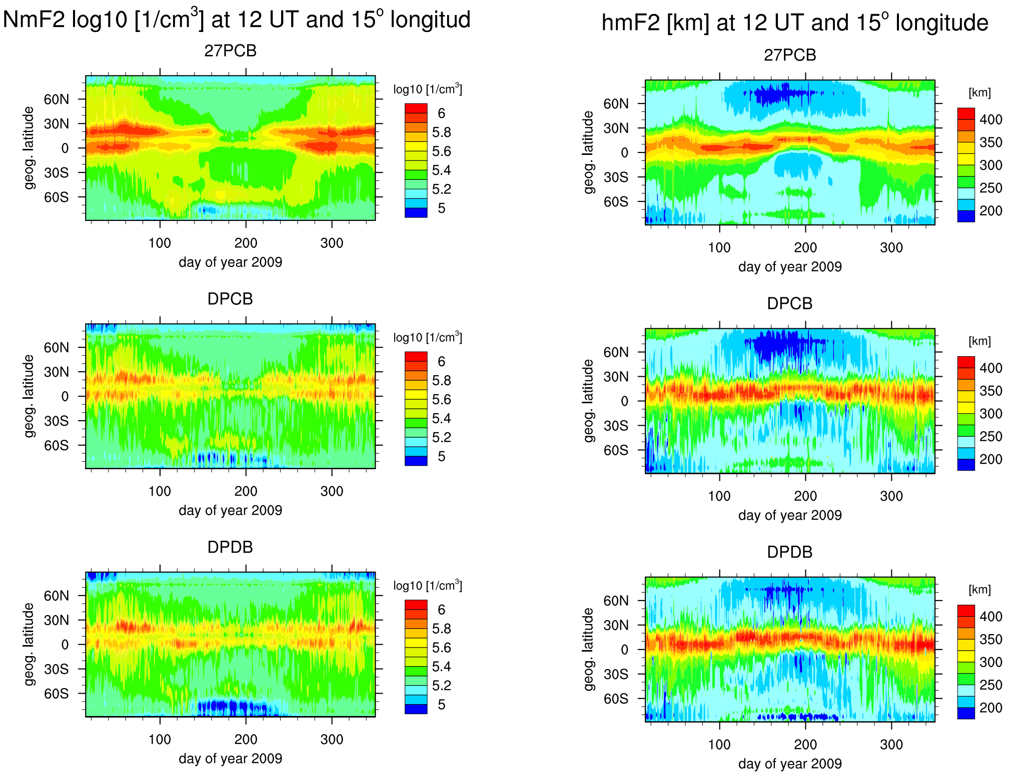

Fig. 11 Latitudinal variation of NmF2 log10 [1/cm3] (left panels) and hmF2 [km] (right panels) at 13 local time for 2009 simulations: 27 day averaged TIMEGCM diurnal perturbation and climatological background (27PCB, top panels), daily TIMEGCM perturbation and climatological background (DPCB, middle panels), and daily TIMEGCM perturbations and background (DPDB, bottom panels).

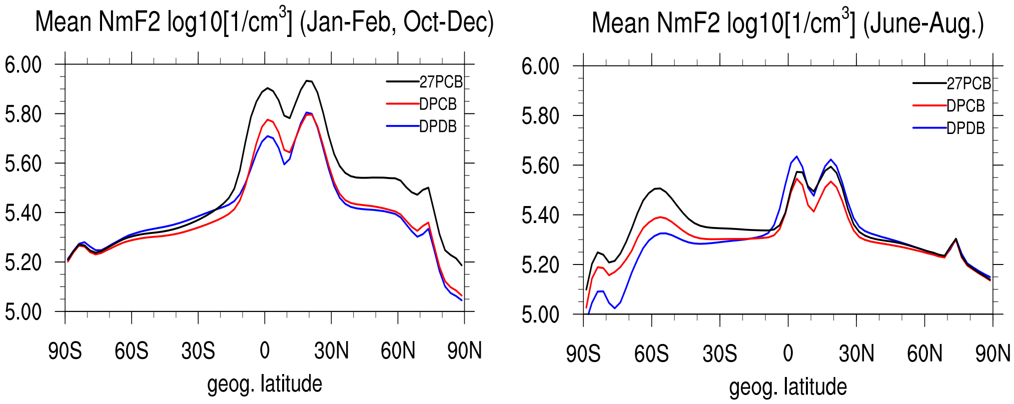

Fig. 12 Mean latitudinal variation of NmF2 log10 [1/cm3] at 13 local time and 15^o geographic longitude (12 UT) for January-February and October-December (left panel), June-August (right panel) for the simulations: 27 day averaged TIMEGCM diurnal perturbation and climatological background (black, 27PCB), daily TIMEGCM perturbation and climatological background (red, DPCB), and daily TIMEGCM perturbations and background (blue, DPDB).

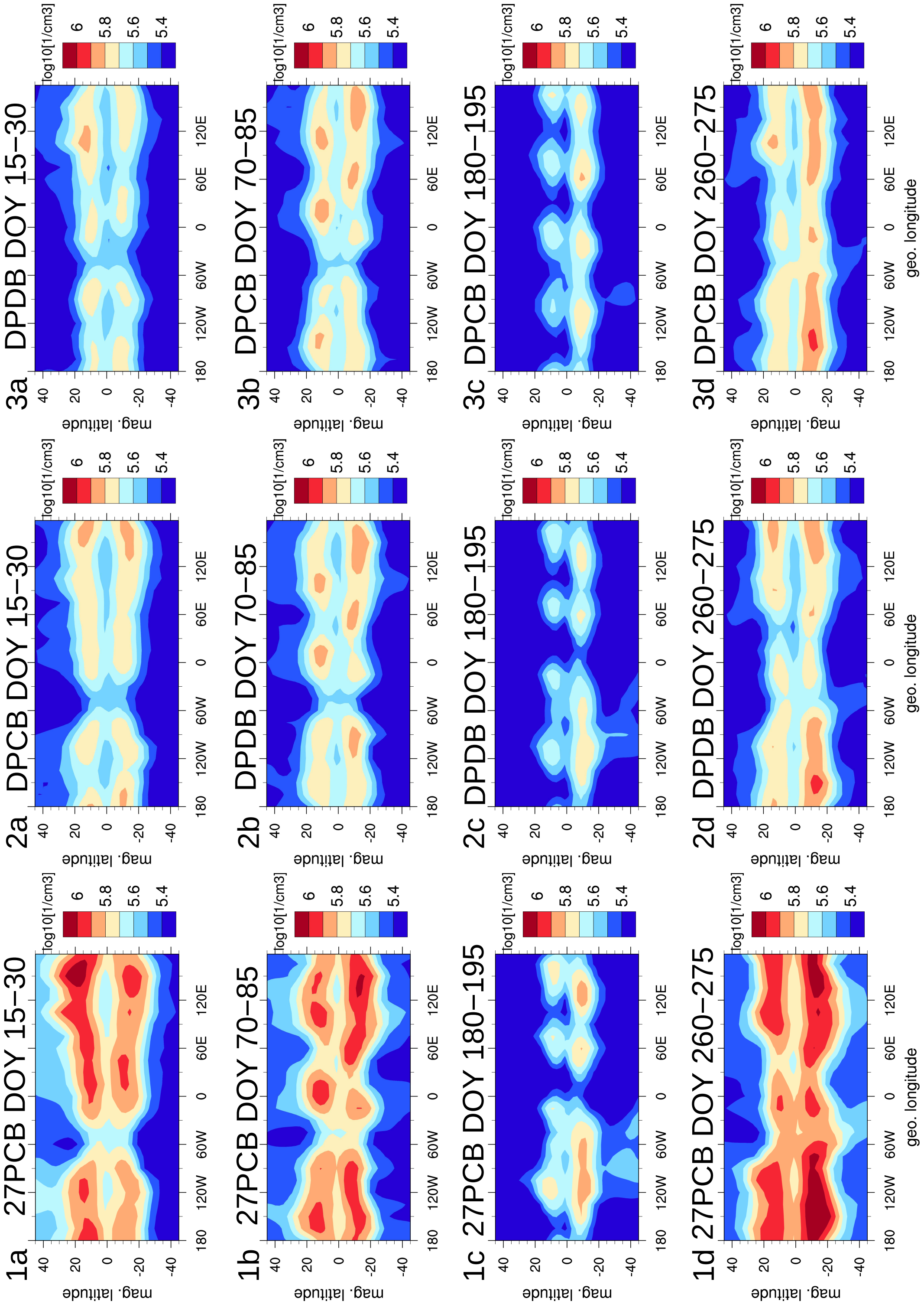

Fig. 13 Variation over magnetic latitudinal and longitude of NmF2 log10 [1/cm3] at 13 local time for 2009 simulations: 27 day averaged TIMEGCM diurnal perturbation and climatological background (1a-1d, left panels, 27PCB); daily TIMEGCM perturbation and climatological background (2a-2d; middle panels, DPCB); daily TIMEGCM perturbations and background (3a=3d, right panels, DPDB). The depicted variations are an 15-day average from day of year (doy) 15-30 (1a, 2a, 3a), doy 70-85 (1b, 2b,3b), doy 180-195 (1c,2c,3c), and doy 260-275 (1d, 2d, 3d).

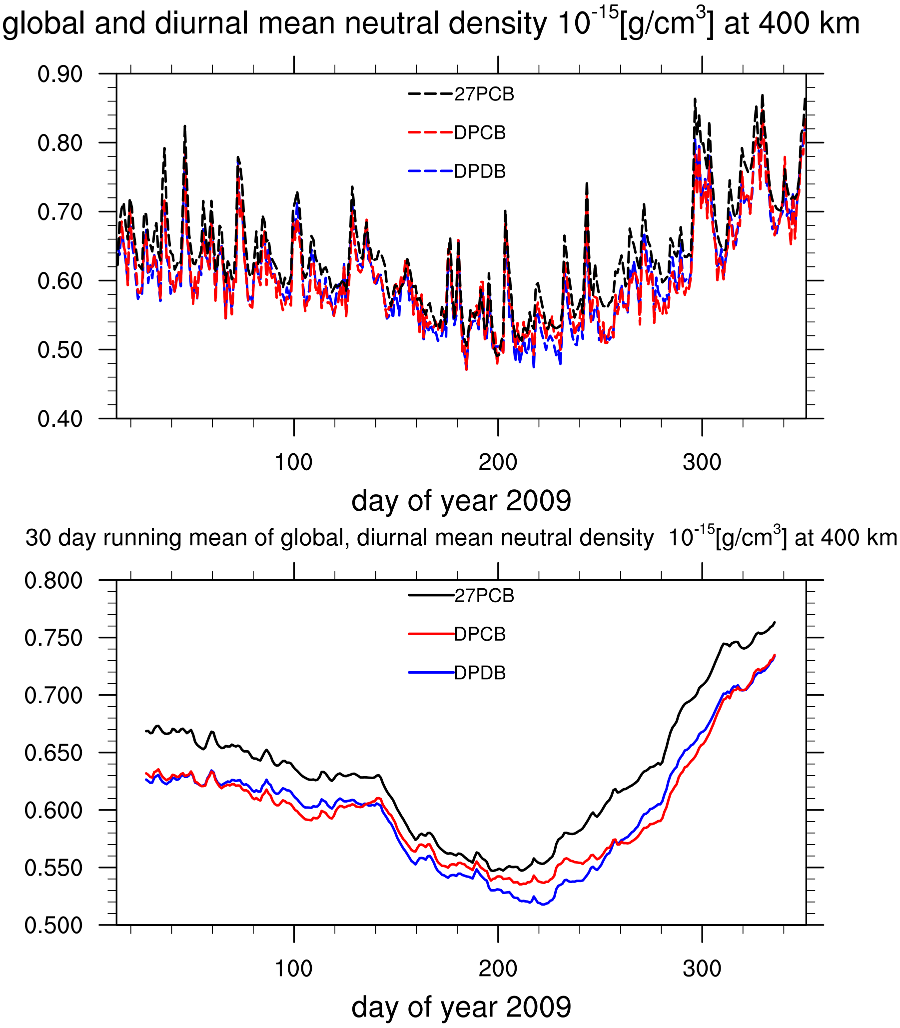

Fig. 14 Global mean neutral density at 400 km for the simulations: 27 day averaged TIMEGCM diurnal perturbation and climatological background (black, 27PCB), daily TIMEGCM perturbation and climatological background (red, DPCB), and daily TIMEGCM perturbations and background (blue, DPDB). The top panels shows the daily mean density and the bottom panels illustrates the 30 day running mean.

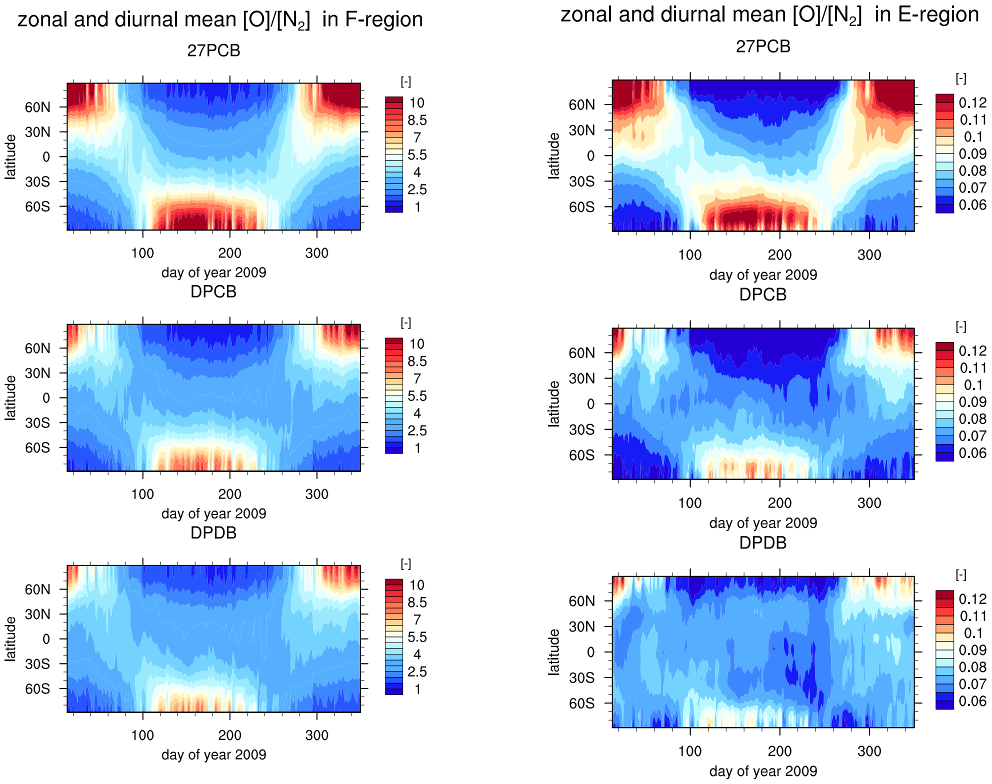

Fig. 15 Zonal and diurnal mean [O]/[N_2] ratio in mass mixing ratio for Z=2.875 (approximately 300km; left panels) and Z=-4.125 (approximately 120 km; right panels) for the simulations: 27 day averaged TIMEGCM diurnal perturbation and climatological background (27PCB, top panels), daily TIMEGCM perturbation and climatological background (DPCB, middle panels), and daily TIMEGCM perturbations and background (DPDB, bottom panels).

F

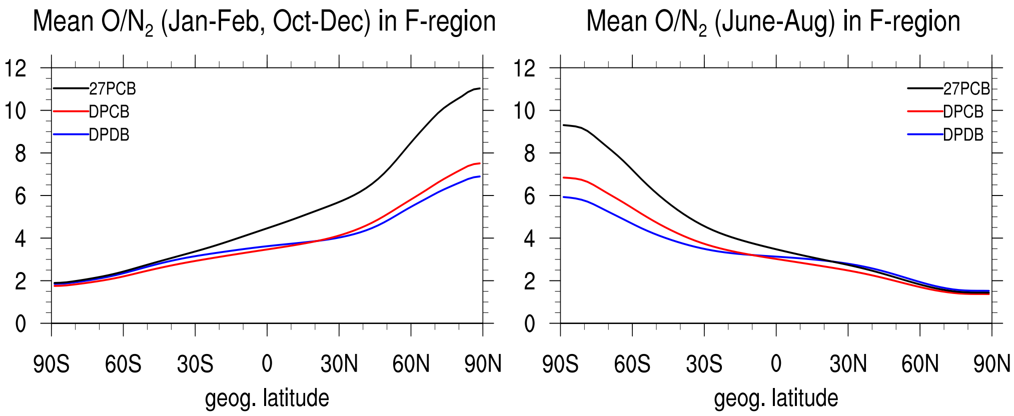

Fig. 16 Mean latitudinal variation of [O]/[N_2] mass mixing ratio [-] for Z=2.875 (approximately 300km) for January-February and October-December (left panel), June-August (right panel) for the simulations: 27 day averaged TIMEGCM diurnal perturbation and climatological background (black, 27PCB), daily TIMEGCM perturbation and climatological background (red, DPCB), and daily TIMEGCM perturbations and background (blue, DPDB).

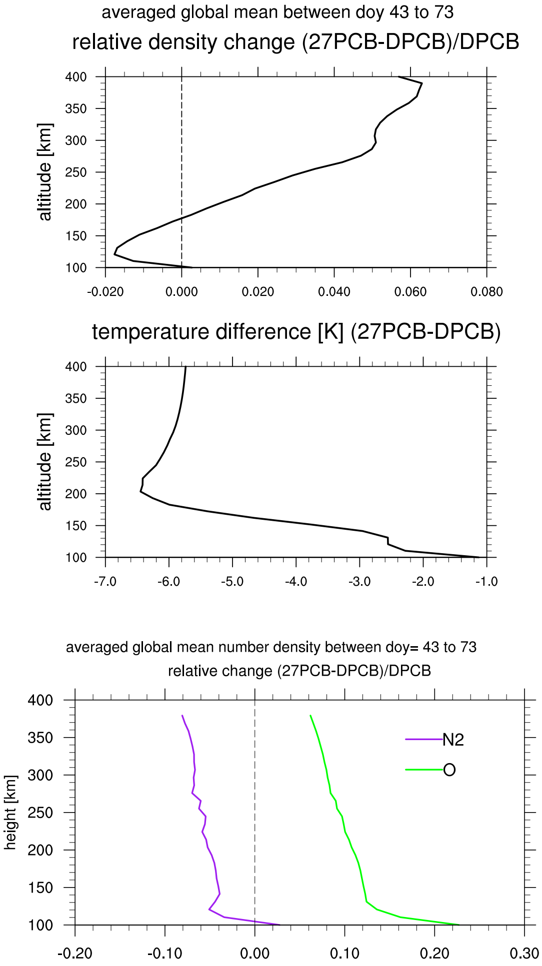

Fig. 17 Global mean height variation for time-averaged profiles between doy 43 to 73: relative change in total neutral density (top), difference in temperature (middle), relative change in O (green) and N2 (purple) number density (bottom) for the 27PCB simulation with respect to DPCB simulation.